

Magnetic superexchange couplings in Sr_2IrO_4 Guoren Zhang¹ and Eva Pavarini^{2,3}¹Key Laboratory of Materials Physics, Institute of Solid State Physics, HFIPS, Chinese Academy of Sciences, Hefei 230031, People's Republic of China²Institute for Advanced Simulation, Forschungszentrum Jülich, 52425 Jülich, Germany³JARA High-Performance Computing, 52056, Aachen, Germany (Received 6 April 2021; revised 27 August 2021; accepted 30 August 2021; published 13 September 2021)

We investigate the magnetic couplings in Sr_2IrO_4 in the Mott-insulating picture, combining density-functional theory, dynamical mean-field theory, and many-body perturbation theory. We first determine the form of the $j_{\text{eff}} = 1/2$ pseudospin via the local-density-approximation + dynamical mean-field theory approach. Next we study the magnetic interactions in the strong-to-intermediate coupling regime. To this end, we calculate the superexchange pseudospin tensors Γ_1 , Γ_2 , and Γ_3 up to fourth order and analyze their dependence on the screened Coulomb interaction integrals U and J . We show that, due to term cancellations, the experimental nearest-neighbor coupling Γ_1 is reasonably well reproduced for a whole range of realistic (U, J) values. We show that increasing the Hund's rule coupling J (within the window of realistic values) can lead to large fourth-order contributions, which could explain the ferromagnetic next-nearest-neighbor coupling Γ_2 extracted from the spin-wave dispersion. This regime is characterized by a sizable ring exchange K . For (U, J) values that yield a Mott insulator with a half-filled $j_{\text{eff}} = 1/2$ state, however, fourth-order terms remain minor even if the gap is small. For no realistic parameters, we find a sizable next-next-nearest-neighbor coupling $\Gamma_3 \sim |\Gamma_2|$. Possible implications are discussed.

DOI: [10.1103/PhysRevB.104.125116](https://doi.org/10.1103/PhysRevB.104.125116)

I. INTRODUCTION

The striking similarities in the electronic properties of Sr_2IrO_4 and La_2CuO_4 fostered the search for superconductivity in doped iridate, making Sr_2IrO_4 the object of intense investigations at the same time [1–8]. Even if superconductivity has not yet been found, other characteristics of cuprates, such as Fermi arcs or the pseudogap [4–6], marginal-Fermi-liquid-like electron scattering rates [7] and electron-boson coupling [8] have been reported. Thus the absence of superconductivity could be of significance by itself, hiding clues about the mechanism for superconductivity in doped La_2CuO_4 ; this is, in particular, true if spin fluctuations play an important role. It is therefore key to study and understand in detail the magnetic interactions in Sr_2IrO_4 , clarify their microscopic origin, and identify the differences with La_2CuO_4 . So far, despite the fact that intense experimental and theoretical work has been devoted to this aim [9–18], important questions remain open. In the first approximation, the magnetic interactions are well described by a two-dimensional antiferromagnetic Heisenberg model in which spins are replaced by $j_{\text{eff}} = 1/2$ pseudospins [1,10]. This reinforces the analogy with cuprates, which, at half filling and low temperature, behave as interacting spin-1/2 systems. In the case of Sr_2IrO_4 , however, the magnetic Hamiltonian immediately appears more complicated. This is due to the microscopic origin of the $j_{\text{eff}} = 1/2$ pseudospin state. The latter emerges from the interplay among spin-orbit coupling, crystal-field splitting, and Coulomb repulsion in an otherwise t_{2g}^5 multiorbital

material. The key magnetic couplings between pseudospins (Γ_α) are displayed in Fig. 1, where each Γ_α is, in principle, a rank 1 tensor. So far, theoretical and experimental estimates [9–18] of the dominant couplings, the diagonal elements of the nearest-neighbor tensor, Γ_1 , vary from 40 meV [16] up to 100 meV [12,19]. Instead, it is an established fact that the SU(2)-symmetry-breaking anisotropy α_{XY} is sizable, $\alpha_{XY} \sim 0.04 - 0.08$ [16–18], differently than in cuprates [20]. Going beyond Γ_1 , the situation becomes even more complex. Fitting the experimental magnon dispersion with linear spin-wave theory requires long-range exchange couplings [15,17,18], which can, in turn, lead to frustration effects under high pressure [21]. More specifically, a ferromagnetic next-nearest-neighbor coupling, Γ_2 , and an antiferromagnetic next-next-nearest-neighbor coupling Γ_3 of similar magnitude have been introduced [15,17,18]. Their nature remains so far unclear, however. They could arise from multiorbital superexchange processes, Coulomb ferromagnetic exchange, or higher order processes, or all that. A ferromagnetic Γ_2 was also proposed for La_2CuO_4 , again to fit experimental spin-wave spectra. In that case, it was, however, suggested that a $\Gamma_2 < 0$ from magnon dispersions could rather be the signature of sizable fourth-order superexchange terms, among which is the ring exchange [22]. Proposals in the same direction have been made, at the model level, also for layered iridate [19]. Still, it remains an open question if high-order superexchange terms indeed play a role for Sr_2IrO_4 . To complicate the matter, extracting relatively small parameters from spin-wave spectra proves difficult [23]; furthermore different spin models

often fit equally well with experimental data, as observed for cuprates [22]. In this situation, materials-specific theoretical investigations are of great help. Although some first-principles calculations have already been performed [14,16], a systematic analysis of all principal superexchange terms, their relative size, and their dependence on the key materials-specific parameters has not been carried out so far.

In this paper, we thus reexamine the problem in a systematic way. To this end, we compute the exchange couplings combining many-body perturbation theory and the local-density approximation+dynamical mean-field theory approach, including explicitly spin-orbit effects (LDA+SO+DMFT). For realistic screened Coulomb parameters (U, J), our LDA+SO+DMFT calculations show that the system is strongly correlated, either in the Mott insulating phase with a small gap or close to the metal-insulator transition. We also find a half-filled $j_{\text{eff}} = 1/2$ multiplet. This confirms the picture emerging from previous theoretical and experimental works [24–35]. In such a situation, the low-energy behavior is well captured by the $j_{\text{eff}} = 1/2$ pseudospin picture and the magnetic exchange couplings between pseudospins can still be obtained via the strong coupling expansion. At the same time, however, orders higher than the second can start to play a role. We thus perform superexchange calculations up to fourth order and analyze the dependence of the interactions on the three key parameters, the crystal-field splitting ε_{CF} , and the screened Coulomb integrals, (U, J).

We show that, for the values of (U, J) that yield the Mott insulating $j_{\text{eff}} = 1/2$ state, second-order superexchange contributions still dominate (strong coupling limit), even if the Mott gap is not very large. Furthermore, due to term cancellations, Γ_1 is comparable with experimental estimates for a whole interval of realistic (U, J) values. In this picture, a small ferromagnetic Γ_2 and an antiferromagnetic Γ_3 of similar size are hard to explain within superexchange theory. This might be an indication that, for a complete description of the magnetic couplings, one needs to include in the model further degrees of freedom, as well as the ferromagnetic Coulomb exchange. Since the experimental charge gap is relatively small, however, another scenario is possible. Going beyond DMFT and taking nonlocal effects into account, a slightly weaker average Coulomb interaction, U_{avg} , could already produce an insulating state. This happens, for example, in the case of the single-band Hubbard model for the cuprates. In the extreme case, Sr_2IrO_4 could be a bad metal with very heavy masses in the paramagnetic phase, becoming an actual insulator only below the magnetic transition [25,34,35]. In such a truly intermediate coupling regime, for sufficiently large J , one could then even obtain a Γ_2 which is both ferromagnetic and comparable with experimental estimates. The reduction in U_{avg} which could produce such an effect is small compared to the one needed for cuprates. In this situation, quantum fluctuations could explain the rest.

The paper is organized as follows. In Sec. II, we describe model and method. In Secs. II A and II B, we present the results of second- and fourth-order superexchange calculations. Conclusions and implications are summarized Sec. III. Additional details are given in the Appendices A and B.

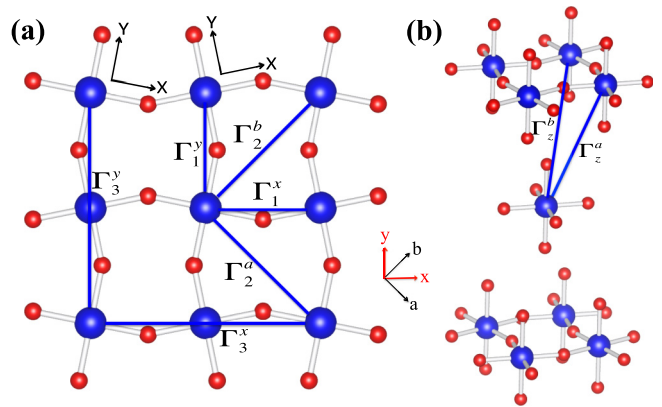


FIG. 1. Sr_2IrO_4 : Most relevant exchange couplings Γ_n^d , where d is the bond direction and n the neighbors' shell. Primitive vectors: $\mathbf{a}, \mathbf{b}, \mathbf{c}$. Global pseudocubic coordinate system: $\mathbf{x} = (\mathbf{a} + \mathbf{b})/2$, $\mathbf{y} = (-\mathbf{a} + \mathbf{b})/2$ and $\mathbf{z} = \mathbf{c}$. Local axes X, Y , and Z , parallel to the Ir-O bonds, are also shown. (a) In-plane couplings $\Gamma_1^{x/y}, \Gamma_2^{a/b}, \Gamma_3^{x/y}$. (b) Interlayer couplings $\Gamma_z^{a/b}$. All couplings are 3×3 tensors with elements $[\Gamma_n^d]_{\alpha,\beta}$; elements α, β are given in the set of axes used to define $j_{\text{eff}} = 1/2$ pseudospin states.

II. METHOD

We first calculate the electronic structure in the local-density approximation with spin-orbit coupling (LDA+SO) via the full-potential linearized augmented plane-wave method implemented in the WIEN2K code [36]. Next we construct the localized t_{2g} Wannier functions centered at the Ir atoms and spanning the t_{2g} bands via projectors and the maximally localized Wannier function method [37,38]. Based on these Wannier orbitals, we build the t_{2g} Hubbard Hamiltonian,

$$\hat{H} = - \sum_{jj'} \sum_{mm'} \sum_{\sigma\sigma'} t_{m\sigma, m'\sigma'}^{j,j'} \hat{c}_{jm\sigma}^\dagger \hat{c}_{j'm'\sigma'} + \frac{1}{2} \sum_j \sum_{mm'pp'} \sum_{\sigma\sigma'} U_{mm'pp'} \hat{c}_{jm\sigma}^\dagger \hat{c}_{j'm'\sigma'}^\dagger \hat{c}_{jp'\sigma'} \hat{c}_{jp\sigma}, \quad (1)$$

where $\hat{c}_{jm\sigma}^\dagger$ ($\hat{c}_{jm\sigma}$) creates (annihilates) an electron at lattice site j with spin $\sigma \in \{\uparrow, \downarrow\}$ and orbital $m \in \{xy, yz, xz\}$. The terms $-t_{m\sigma, m'\sigma'}^{j,j'}$ give the on-site crystal-field matrix ($j = j'$) and intersite hopping integrals ($j \neq j'$). The spin-orbit interaction enters both in the on-site term and in the hopping integrals. The parameters $U_{mm'pp'}$ are elements of the screened Coulomb interaction tensor. The essential terms for t_{2g} electrons are [39] the direct Coulomb interaction, $U_{mm'mm'} = U_{m,m'} = U - 2J(1 - \delta_{m,m'})$, the exchange Coulomb term $U_{mm'm'm} = J$, the pair-hopping interaction, $U_{mm'm'm'} = J$, and the spin-flip term $U_{mm'm'm} = J$. Estimates from constrained random-phase approximation (cRPA) calculations [24–26,40] yield $U \sim 2.0 - 2.6$ eV and $J \sim 0.15 - 0.3$ eV. Keeping in mind that cRPA is not exact and can overestimate screening, we perform calculations for an interval of parameters around and slightly above these numbers.

For setting up the Hamiltonian, we first introduce t_{2g} Wannier functions in the global pseudocubic axes, shown in Fig. 1, and order them as $|xy\rangle_\uparrow, |yz\rangle_\uparrow, |xz\rangle_\uparrow, |xy\rangle_\downarrow, |yz\rangle_\downarrow, |xz\rangle_\downarrow$. It is convenient to change basis to $|XY\rangle_\sigma^j = e^{-i\sigma\alpha_s^j} |xy\rangle_\sigma, |YZ\rangle_\sigma^j =$

$e^{-i\sigma\alpha_s^j}|y\alpha_0^j z\rangle_\sigma$, and $|XZ\rangle_\sigma^j = e^{-i\sigma\alpha_s^j}|x\alpha_0^j z\rangle_\sigma$, where $\sigma = \pm 1/2$, while $y\alpha_0^j = y \cos \alpha_0^j - x \sin \alpha_0^j$ and $x\alpha_0^j = y \sin \alpha_0^j + x \cos \alpha_0^j$ with the constraint

$$\alpha_0^j + \alpha_s^j = \alpha_c^j = -\text{atan} \frac{\text{Im}\langle xy, \uparrow | \hat{h}_{\text{SO}} | yz, \downarrow \rangle_j}{\text{Re}\langle xy, \uparrow | \hat{h}_{\text{SO}} | yz, \downarrow \rangle_j}, \quad (2)$$

where \hat{h}_{SO} is the local part of the spin-orbit interaction. Due to the alternate rotations of corner-sharing IrO_6 octahedra, the couple (α_0^j, α_s^j) at nearest-neighboring Ir sites in the plane has opposite sign, $(\alpha_0^j, \alpha_s^j) = \text{sign}_j \times (\alpha_0, \alpha_s)$. The angle $\alpha_0 \sim 14^\circ$ is close to a rotation to local axes, labeled X and Y in Fig. 1. Such a transformation brings the on-site one-electron part of the Hamiltonian in the S_4 -symmetric form

$$\varepsilon = \begin{pmatrix} \varepsilon_{XY} & 0 & 0 & 0 & \frac{\lambda_Y}{2} & -\frac{i\lambda_X}{2} \\ 0 & \varepsilon_{YZ} & \frac{i\lambda_Z}{2} & -\frac{\lambda_Y}{2} & 0 & 0 \\ 0 & -\frac{i\lambda_Z}{2} & \varepsilon_{XZ} & \frac{i\lambda_X}{2} & 0 & 0 \\ 0 & -\frac{\lambda_Y}{2} & -\frac{i\lambda_X}{2} & \varepsilon_{XY} & 0 & 0 \\ \frac{\lambda_Y}{2} & 0 & 0 & 0 & \varepsilon_{YZ} & -\frac{i\lambda_Z}{2} \\ \frac{i\lambda_X}{2} & 0 & 0 & 0 & \frac{i\lambda_Z}{2} & \varepsilon_{XZ} \end{pmatrix}, \quad (3)$$

where $\varepsilon_{M\sigma, M'\sigma'} = -t_{M\sigma, M'\sigma'}^{j,j}$. The energies ε_{XY} , ε_{YZ} , and ε_{XZ} are the crystal-field energies, with $\varepsilon_{YZ} = \varepsilon_{XZ}$. We define the crystal-field splitting as $\varepsilon_{\text{CF}} = (\varepsilon_{YZ} + \varepsilon_{XZ})/2 - \varepsilon_{XY}$. The couplings λ_X , λ_Y , and λ_Z are the spin-orbit (SO) matrix elements; due to S_4 symmetry, $\lambda_Y = \lambda_X$. For the experimental structure [41], we obtain in LDA $\lambda_{X/Y} \sim 346$ meV, $\lambda_Z \sim 354$ meV, and $\varepsilon_{\text{CF}} \sim 213$ meV. A positive ε_{CF} is not what one expects from a naive model based on elongated IrO_6 octahedra [42]; in the literature, the adopted value of ε_{CF} thus varies from -202 meV [43] to 360 meV [44,45]. For this reason, we will study the effects of varying ε_{CF} in an interval including both positive and negative values. In the t_{2g}^5 atomic-limit configuration, the hole goes in the Kramers doublet,

$$|\sigma\rangle^j = i\alpha_6 |XY^h\rangle_\sigma^j - \alpha_5 \frac{|XZ^h\rangle_\sigma^j - 2i\sigma |YZ^h\rangle_\sigma^j}{\sqrt{2}}, \quad (4)$$

where $|M^h\rangle_\sigma^j$ is a t_{2g}^5 multiplet with one hole in orbital $|M\rangle_\sigma^j$, while α_6 and α_5 are positive real numbers and $\alpha_6^2 + \alpha_5^2 = 1$. In Appendix A, we give the expression and energies of all atomic t_{2g}^5 multiplets. The expression Eq. (4) defines the effective $j_{\text{eff}} = 1/2$ state. For the $j_{\text{ideal}} = 1/2$ state (zero crystal-field splitting), $\alpha_5^2 = 2/3 \sim 0.667$. Using the LDA crystal-field matrix, one obtains $\alpha_5^2 \sim 0.812$ in the atomic limit. In terms of the original basis, Eq. (4) can be reexpressed as

$$\begin{aligned} |\sigma\rangle^j &= e^{-i\sigma\alpha_s^j} |\tilde{\sigma}\rangle^j, \\ |\tilde{\sigma}\rangle^j &= \left(i\alpha_6 |xy^h\rangle_\sigma^j - \alpha_5 e^{+2i\sigma\alpha_s^j} \frac{|xz^h\rangle_\sigma^j - 2i\sigma |yz^h\rangle_\sigma^j}{\sqrt{2}} \right). \end{aligned} \quad (5)$$

Starting from Hamiltonian Eq. (1), we first perform many-body calculations based on the local-density-approximation + dynamical mean-field theory, fully accounting for the spin-orbit interaction (LDA+SO+DMFT). We adopt as the quantum impurity solver the interaction-expansion quantum Monte Carlo approach, in the implementation presented in Refs. [46–51]. Calculations are carried out in the t_{2g} basis with a 6×6 self-energy matrix in spin-orbital space with

off-diagonal elements; they are performed in the paramagnetic phase.

Previous DMFT-based studies based on cRPA Coulomb parameters indicate that the system is strongly correlated, although not deep in the Mott regime [24–26]. This finds confirmation in experiments, as one may see, e.g., from Refs. [31,34]. Our results support this scenario. Due to the relative proximity to the Mott transition, the exact U value for which, in theoretical simulations, the gap opens depends on details of the modeling and the approximation adopted, either in the solution method or at the stage of model building. Our calculations, performed for the t_{2g} Hubbard model Eq. (1) with full Coulomb vertex and self-energy matrix, yield a Mott gap of about 0.4 eV for, e.g., both for $(U, J) = (3.2, 0.4)$ eV $(U, J) = (2.4, 0)$ eV. Such a gap is close to the one reported in various experiments [27–33]. For $(U, J) = (2.0, 0)$ we find a pseudogap at $T = 1/20$ eV, indicating that the system is still metallic but close to the Mott transition. Finally, for all realistic (U, J) parameters, we find a half-filled $j_{\text{eff}} = 1/2$ pseudospin ground state, defined in Eq. (4). In the Mott phase, this state is very close to the one obtained in the atomic limit for the LDA value of the crystal-field splitting. In such a strong-to-intermediate coupling regime, the magnetic interactions can be obtained in the $j_{\text{eff}} = 1/2$ picture via strong-coupling perturbation theory; at the same time, however, fourth-order terms can start to play a role.

By performing superexchange calculations up to fourth order, we obtain a generalized Heisenberg-like model for pseudospins, \hat{H}_{SE} , discussed in the next sections. Here we would like to add only a remark. \hat{H}_{SE} includes, in principle, a Dzyaloshinskii-Moriya (DM) [52] term; since the xy plane is almost a mirror, for an in-plane pair of Ir ions, in practice, the only nonzero element of the DM vector is the axial component, $\mathbf{D}^{j,j'} = (0, 0, [D^{j,j'}]_z)$. By a staggered rotation of the pseudospins, defined via the angle α_s^j in Eq. (5), the Hamiltonian with axial DM interaction can be mapped into an equivalent anisotropic Heisenberg model [10]. In the case of SrIr_2O_4 , we find that, at second order, this is obtained for $\alpha_s \sim -1.2^\circ$ ($\alpha_0 \sim 14^\circ$), as shown in Fig. 2. This result can be understood in a simple way if we set the Hund's rule coupling $J = 0$. Then

$$[D^{j,j'}]_z = \frac{2i}{U} \left(t_{\downarrow, \downarrow}^{j,j'} \overline{t_{\uparrow, \uparrow}^{j,j'}} - t_{\uparrow, \uparrow}^{j,j'} \overline{t_{\downarrow, \downarrow}^{j,j'}} \right). \quad (6)$$

For the hopping integrals in Table I, obtained for $\alpha_s \sim -1.2^\circ$, the DM coupling vanishes. In the rest of the paper, we adopt this staggered rotation for pseudospins. In this basis, the only remaining DM coupling is the small term arising from fourth-order contributions; hence we will not further discuss the DM interaction.

A. Second-order terms

The second-order superexchange Hamiltonian has the form $\hat{H}_{\text{SE}} = \frac{1}{2} \sum_{j,j'} \hat{H}_{\text{SE}}^{j,j'}$. Assuming as ground multiplet the pseudospin $\tilde{\mathbf{S}}_j$ defined in Eq. (5), we obtain the superexchange Hamiltonian from the 4×4 second-order energy-gain matrix, $\mathcal{M}_{j,j'}^{(2)}$. As a matter of fact,

$$\hat{H}_{\text{SE}}^{j,j'} = \tilde{\mathbf{S}}_j^T \Gamma^{j,j'} \tilde{\mathbf{S}}_{j'} \longrightarrow \mathcal{M}_{j,j'}^{(2)} - \frac{1}{4} \text{Tr}[\mathcal{M}_{j,j'}^{(2)}], \quad (7)$$

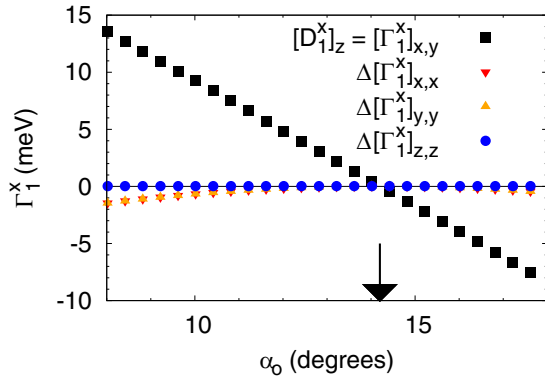


FIG. 2. Nearest-neighbor Dzyaloshinskii-Moriya interaction $[D_1^x]_z$ for a bond along \hat{x} as a function of the angle α_0 , second-order perturbation theory. Also shown are the deviations of the diagonal elements of the Γ_1 tensor from their values for $\alpha_0 \sim 14^\circ$ (indicated with an arrow). The reference values are (in meV) 63.9, 62.6, and 59.9 for components (x, x) , (y, y) , and (z, z) , respectively. Calculation are for $U = 3.2$ eV and $J = 0.4$ eV. Similar conclusions are reached for $U = 2.0$ eV.

where the right-hand side is the operator expressed in matrix form, in the basis of the pseudospins. For Hund's rule coupling $J = 0$, the general form of the diagonal superexchange couplings for a single-band $j_{\text{eff}} = 1/2$ mode is

$$[\Gamma^{j,j'}]_{xx} = 2 \frac{t_{\uparrow,\uparrow}^{j,j'} \overline{t_{\downarrow,\downarrow}^{j,j'}} + t_{\downarrow,\downarrow}^{j,j'} \overline{t_{\uparrow,\uparrow}^{j,j'}} + t_{\uparrow,\downarrow}^{j,j'} \overline{t_{\downarrow,\uparrow}^{j,j'}} + t_{\downarrow,\uparrow}^{j,j'} \overline{t_{\uparrow,\downarrow}^{j,j'}}}{U}, \quad (8)$$

$$[\Gamma^{j,j'}]_{yy} = 2 \frac{t_{\uparrow,\uparrow}^{j,j'} \overline{t_{\downarrow,\downarrow}^{j,j'}} + t_{\downarrow,\downarrow}^{j,j'} \overline{t_{\uparrow,\uparrow}^{j,j'}} - t_{\uparrow,\downarrow}^{j,j'} \overline{t_{\downarrow,\uparrow}^{j,j'}} - t_{\downarrow,\uparrow}^{j,j'} \overline{t_{\uparrow,\downarrow}^{j,j'}}}{U}, \quad (9)$$

$$[\Gamma^{j,j'}]_{zz} = 2 \frac{t_{\uparrow,\uparrow}^{j,j'} \overline{t_{\uparrow,\uparrow}^{j,j'}} + t_{\downarrow,\downarrow}^{j,j'} \overline{t_{\downarrow,\downarrow}^{j,j'}} - t_{\uparrow,\downarrow}^{j,j'} \overline{t_{\downarrow,\uparrow}^{j,j'}} - t_{\downarrow,\uparrow}^{j,j'} \overline{t_{\uparrow,\downarrow}^{j,j'}}}{U}. \quad (10)$$

Here the labels \uparrow and \downarrow denote the pseudospin states. These couplings are isotropic for Sr_2IrO_4 , as one can see inserting in the formulas the hopping integrals from Table I; the

TABLE I. Hopping integrals $t_{\sigma,\sigma'}^{j,j'}$ between site j and $j' \sim j + l\mathbf{x} + m\mathbf{y} + n\mathbf{z}$ in meV. The global pseudocubic axes are defined as $\mathbf{x} = \frac{1}{2}(\mathbf{a} + \mathbf{b})$, $\mathbf{y} = \frac{1}{2}(-\mathbf{a} + \mathbf{b})$, $\mathbf{z} = \mathbf{c}$. The quantum numbers σ and σ' denote the pseudospin quantum numbers. Pseudospins at site j are rotated about the \hat{z} by the angle $\alpha_s^j = \text{sign}_j \times \alpha_s$ with $\alpha_s = -1.2^\circ$.

Due to time-reversal symmetry, $t_{\uparrow,\uparrow}^{j,j'} = \overline{t_{\downarrow,\downarrow}^{j,j'}}$ and $t_{\uparrow,\downarrow}^{j,j'} = -\overline{t_{\downarrow,\uparrow}^{j,j'}}$; because of the S_4 symmetry of Ir sites, one can show that the latter are zero within a plane.

lmn	$t_{\uparrow,\uparrow}^{j,j'}$	$t_{\uparrow,\downarrow}^{j,j'}$	$t_{\downarrow,\uparrow}^{j,j'}$	$t_{\downarrow,\downarrow}^{j,j'}$
100	(-198,0)	(0,0)	(0,0)	(-198,0)
010	(-198,0)	(0,0)	(0,0)	(-198,0)
1-10	(-19,0)	(0,0)	(0,0)	(-19,0)
110	(-19,0)	(0,0)	(0,0)	(-19,0)
200	(1,0)	(0,0)	(0,0)	(1,0)
020	(1,0)	(0,0)	(0,0)	(1,0)

anisotropy appears for finite J [10]. The off-diagonal terms of the tensor are instead given by

$$[\Gamma^{j,j'}]_{xy} = 2i \frac{-t_{\uparrow,\uparrow}^{j,j'} \overline{t_{\downarrow,\downarrow}^{j,j'}} + t_{\downarrow,\downarrow}^{j,j'} \overline{t_{\uparrow,\uparrow}^{j,j'}} + t_{\uparrow,\downarrow}^{j,j'} \overline{t_{\downarrow,\uparrow}^{j,j'}} - t_{\downarrow,\uparrow}^{j,j'} \overline{t_{\uparrow,\downarrow}^{j,j'}}}{U}, \quad (11)$$

$$[\Gamma^{j,j'}]_{yx} = 2i \frac{+t_{\uparrow,\uparrow}^{j,j'} \overline{t_{\downarrow,\downarrow}^{j,j'}} - t_{\downarrow,\downarrow}^{j,j'} \overline{t_{\uparrow,\uparrow}^{j,j'}} + t_{\uparrow,\downarrow}^{j,j'} \overline{t_{\downarrow,\uparrow}^{j,j'}} - t_{\downarrow,\uparrow}^{j,j'} \overline{t_{\uparrow,\downarrow}^{j,j'}}}{U}, \quad (12)$$

$$[\Gamma^{j,j'}]_{xz} = 2 \frac{+t_{\uparrow,\uparrow}^{j,j'} \overline{t_{\downarrow,\downarrow}^{j,j'}} - t_{\downarrow,\downarrow}^{j,j'} \overline{t_{\uparrow,\uparrow}^{j,j'}} - t_{\uparrow,\downarrow}^{j,j'} \overline{t_{\downarrow,\uparrow}^{j,j'}} + t_{\downarrow,\uparrow}^{j,j'} \overline{t_{\uparrow,\downarrow}^{j,j'}}}{U}, \quad (13)$$

$$[\Gamma^{j,j'}]_{zx} = 2 \frac{+t_{\uparrow,\uparrow}^{j,j'} \overline{t_{\downarrow,\downarrow}^{j,j'}} - t_{\downarrow,\downarrow}^{j,j'} \overline{t_{\uparrow,\uparrow}^{j,j'}} + t_{\uparrow,\downarrow}^{j,j'} \overline{t_{\downarrow,\uparrow}^{j,j'}} - t_{\downarrow,\uparrow}^{j,j'} \overline{t_{\uparrow,\downarrow}^{j,j'}}}{U}, \quad (14)$$

$$[\Gamma^{j,j'}]_{yz} = 2i \frac{+t_{\uparrow,\uparrow}^{j,j'} \overline{t_{\downarrow,\downarrow}^{j,j'}} + t_{\downarrow,\downarrow}^{j,j'} \overline{t_{\uparrow,\uparrow}^{j,j'}} - t_{\uparrow,\downarrow}^{j,j'} \overline{t_{\downarrow,\uparrow}^{j,j'}} - t_{\downarrow,\uparrow}^{j,j'} \overline{t_{\uparrow,\downarrow}^{j,j'}}}{U}, \quad (15)$$

$$[\Gamma^{j,j'}]_{zy} = 2i \frac{-t_{\uparrow,\uparrow}^{j,j'} \overline{t_{\downarrow,\downarrow}^{j,j'}} - t_{\downarrow,\downarrow}^{j,j'} \overline{t_{\uparrow,\uparrow}^{j,j'}} + t_{\uparrow,\downarrow}^{j,j'} \overline{t_{\downarrow,\uparrow}^{j,j'}} + t_{\downarrow,\uparrow}^{j,j'} \overline{t_{\uparrow,\downarrow}^{j,j'}}}{U} \quad (16)$$

and they are all zero. For $J = 0$, the hopping integrals to excited $j_{\text{eff}} = 3/2$ states do not contribute at second order. Going back to realistic Coulomb parameters, for $(U, J) = (3.2, 0.4)$ eV, values giving the experimental gap in LDA+SO+DMFT, we thus find

$$\Gamma_1^x = \begin{pmatrix} 63.9 & 0.0 & 0.0 \\ 0.0 & 62.6 & 0.0 \\ 0.0 & 0.0 & 59.9 \end{pmatrix} \text{meV}. \quad (17)$$

This is the matrix for a bond along the x direction (Fig. 1); the one for an analogous bond along the y can be obtained exchanging the first two diagonal components of Γ_1^x . Reducing U to 2.0 eV, a representative cRPA value, keeping everything else the same, we find instead

$$\Gamma_1^x = \begin{pmatrix} 132.5 & 0.0 & 0.0 \\ 0.0 & 128.6 & 0.0 \\ 0.0 & 0.0 & 120.2 \end{pmatrix} \text{meV}. \quad (18)$$

From these matrices, we can extract the anisotropy,

$$\alpha_{XY} = \frac{[\Gamma_1]_{\perp} - [\Gamma_1]_{\parallel}}{[\Gamma_1]_{\perp}}, \quad (19)$$

where $[\Gamma_1]_{\parallel} = \Gamma_{1z}$ and $[\Gamma_1]_{\perp} = ([\Gamma_1^{x/y}]_{x,x} + [\Gamma_1^{x/y}]_{y,y})/2$; we obtain $\alpha_{XY} \sim 0.05$ for $U = 3.2$ eV and $\alpha_{XY} \sim 0.09$ for $U = 2.0$ eV. Up to this point, the form of the superexchange Hamiltonian is similar to the one introduced in Ref. [10], including the sign of the anisotropy.

The average diagonal coupling extracted from fitting spin-wave spectra is $\Gamma_1 \sim 60$ meV; hence the agreement is very good for $U = 3.2$ eV, while the calculated couplings are about a factor two too large for $U = 2.0$ eV. For what concerns the anisotropy, the numbers obtained are all in line with experimental estimates [15,17,18].

Next we consider the matrix of next-nearest neighbor couplings (Γ_2) along \mathbf{a} , finding for $U = 3.2$ eV

$$\Gamma_2^a = \begin{pmatrix} 0.5 & 0.0 & 0.0 \\ 0.0 & 0.2 & 0.0 \\ 0.0 & 0.0 & 1.0 \end{pmatrix} \text{meV}, \quad (20)$$

TABLE II. Exchange couplings (in meV) obtained in second- and fourth-order perturbation theory calculations. Coulomb parameters: $U = 3.2$ eV, $U = 2.0$ eV, $J = 0.4$ eV. When relevant, for the second-order terms, $\Gamma^{(2)}$, we give all three diagonal elements in the format $([\Gamma]_{x,x}, [\Gamma]_{y,y}, [\Gamma]_{z,z})$. Fourth-order terms are approximately isotropic. Values calculated excluding the contribution of spin-orbit excitonic states are given in a separate column. The total couplings are defined as $\Gamma_{\text{tot}} = \frac{1}{3}\text{Tr}[\Gamma^{(2)}] + \Gamma^{(4)}$. We keep the K term separate here since, although it modifies the actual total couplings, its contribution cannot be extracted from linear spin-wave dispersions.

	U	Order	Γ_1^x	No excitons	Γ_2^a	No excitons	Γ_3^x	No excitons	$\Gamma_z^{a/b}$	K
Γ_{tot}	3.2	$\Gamma^{(2)}$	(63.9, 62.6, 59.9)		(0.5, 0.2, 1.0)		0.0		0.0	–
	3.2	$\Gamma^{(4)}$	–3.8	–6.4	–0.4	1.7	–0.5	0.5	–	4.3
	3.2		58.3	55.7	0.2	–1.1	–0.5	0.5	–	4.3
	2.0	$\Gamma^{(2)}$	(132.5, 128.6, 120.2)		(1.0, 0.1, 2.4)		0.0		0.0	–
Γ_{tot}	2.0	$\Gamma^{(4)}$	–54.8	–64.8	–15.5	–20.0	0.87	4.5	–	40.2
	2.0		72.3	62.3	–14.3	–18.8	0.87	4.5	–	40.2
Γ_{exp}			60 [15]		–20 [15]		15 [15]		–	–
			57 [17]		–18 [17]		14 [17]		–	–
			57 [18]		–16.5 [18]		12.4 [18]		–	–
			100 [12]		–		–		–	–

and for $U = 2.0$ eV

$$\Gamma_2^a = \begin{pmatrix} 1.0 & -0.2 & 0.0 \\ -0.2 & 0.1 & 0.0 \\ 0.0 & 0.0 & 2.4 \end{pmatrix} \text{meV}. \quad (21)$$

The couplings along \mathbf{b} can be obtained exchanging the first two diagonal components of Γ_2^a . The tensors Eqs. (20) and (21) show that the average Γ_2 is antiferromagnetic and relatively small in absolute value, a result in sharp contrast with the estimates obtained by fitting the magnon dispersion [15,17,18]. The latter is ferromagnetic and about -18 meV, more than an order of magnitude larger (in absolute value) than the calculated values. Finally, the interplane matrices Γ_z^a and Γ_z^b have elements very close to zero in all cases.

The most relevant second-order superexchange couplings are summarized in Table II. The discrepancies found so far could of course come from the choice of Coulomb parameters, and, in particular, the Hund's rule coupling J . This is investigated in Fig. 3. The figure shows that Γ_1 increases with increasing J . This can be understood in a simple way; for the

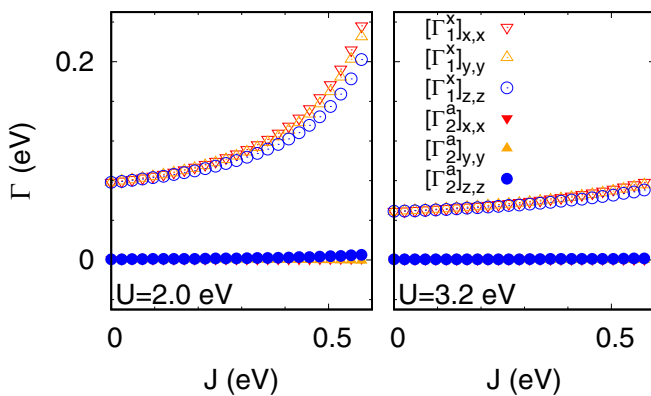


FIG. 3. Diagonal elements of the superexchange couplings Γ_1 and Γ_2 for two representative U values and as a function of the Hund's rule coupling J . The cRPA estimates are $J \sim 0.15 - 0.3$ eV [24–26,40].

$j_{\text{ideal}} = 1/2$ state (zero crystal field splitting), the virtual excitation with two electrons in the $j_{\text{ideal}} = 1/2$ state has energy $U - 4/3J$ (see Ref. [48]), hence the associated superexchange coupling increases with increasing J . For $U = 3.2$ eV, the changes obtained increasing J from 0.2 eV to 0.4 eV, the realistic interval, is small, however. The change is larger for $U = 2.0$ eV. In this case for $J = 0.2$ eV, we obtain $\Gamma_1 \sim 90$ meV; this is sizably smaller than for $J = 0.4$ eV, which yields $\Gamma_1 \sim 130$ meV, but still too large compared to the experimental spin-wave bandwidth. Agreement can only be recovered for $J \rightarrow 0$. Figure 3 shows that the relative strength of Γ_1 and Γ_2 does not change much with the Coulomb parameters; Γ_2 remain always much smaller than Γ_1 in absolute value. Furthermore, it stays positive (i.e., antiferromagnetic) for all realistic U and J values. Hence, modifications of J in an interval of possible realistic values does not change the picture. The second source of uncertainty is the value of the crystal-field splitting ε_{CF} , for which both positive and negative values have been adopted in the literature. This effect is analyzed in Fig. 4, where we vary ε_{CF} (and thus also the effective pseudospin) while keeping all the rest the same. We find that a negative ε_{CF} increases the isotropic part of Γ_1 , while the opposite happens for a positive ε_{CF} . In Sr_2IrO_4 , in LDA we obtain $\varepsilon_{\text{CF}} \sim 0.2$ eV, positive; for such value, agreement with experimental Γ_1 is best reached for $U \sim 3.2$ eV, as already mentioned; a crystal field of the same size but opposite sign would lead to a too large coupling. Instead, for $U = 2.0$ eV an unrealistically large positive splitting would be needed for finding good agreement with experiment, even if at the same time we reduce J to 0.2 eV.

For what concerns the anisotropy, Fig. 4 shows that α_{XY} starts to increase at $\varepsilon_{\text{CF}} \sim -0.3$ eV, where $\alpha_6 \sim \alpha_5$ and the dominant component changes. The anisotropy is finite even for $\varepsilon_{\text{CF}} = 0$ (vertical dotted line), corresponding in the atomic limit to the $j_{\text{ideal}} = 1/2$ state [10]. The agreement remains good in the whole range shown for positive crystal-field splitting. All these results thus support $\varepsilon_{\text{CF}} > 0$, as found in LDA. In the bottom panel of Fig. 4, we analyze the effect of the crystal-field splitting on Γ_2 . We show results for $U = 2.0$ eV, but the same conclusion can be reached for a larger U . The figure shows that, no matter the value of ε_{CF} (within a realistic

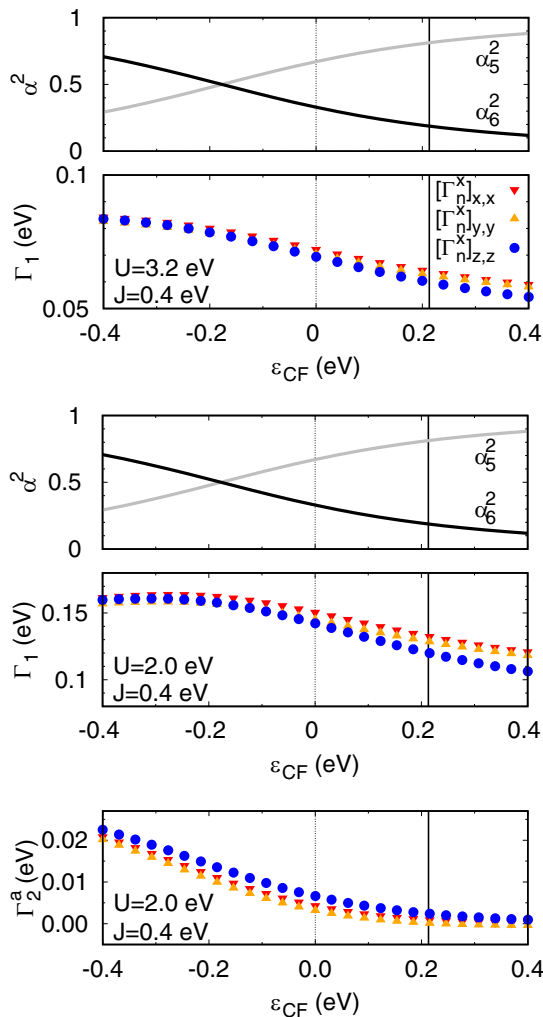


FIG. 4. Top and center panel: Components of the pseudospin, α_5^2 and α_6^2 and exchange parameters Γ_1 as a function of the crystal-field splitting ε_{CF} . Vertical lines: Ideal $j = 1/2$ state with zero crystal-field splitting (dashed) and LDA+SO crystal-field splitting for the experimental structure (full). Top: $U = 3.2$ eV. Center: $U = 2.0$ eV. Bottom panel: Variation of Γ_2 with ε_{CF} , $U = 2.0$ eV, $J = 0.4$ eV.

interval), the coupling remains antiferromagnetic (positive), contrarily to experimental estimates.

In Fig. 5, we show the spin-wave spectra obtained in linear spin-wave theory with the parameters calculated so far, compared to experiments. The top left panel of the figure shows that the bandwidth is approximately of the right order for $(U, J) = (3.2, 0.4)$ eV but the dispersion differs, as can be seen along XM . For $U = 2.0$ eV, instead, unless J is unrealistically small and the crystal field very large, the value of Γ_1 is too large, and the overall agreement is poor. The good agreement shown in the top right panel of the figure is obtained for the parameters estimated from fitting spin-waves in Ref. [18]; here Γ_1 is close to the value obtained for $(U, J) = (3.2, 0.4)$ eV or $(U, J) = (2.4, 0.0)$ eV. The figure shows that, in addition, a ferromagnetic Γ_2 and an antiferromagnetic Γ_3 , comparable in absolute value, are needed in linear spin-wave theory for recovering full agreement with experiments.

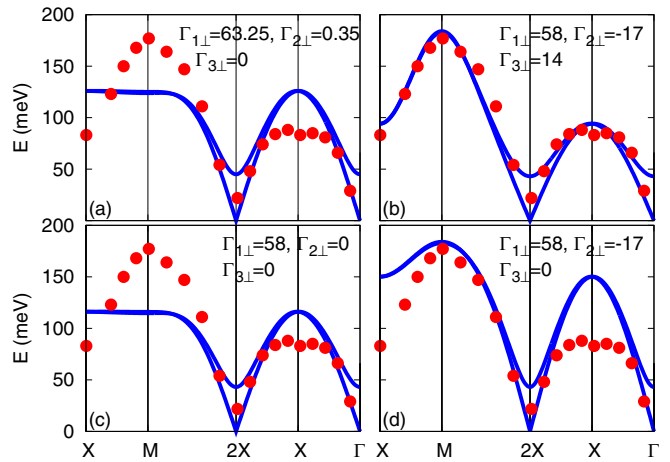


FIG. 5. Theoretical spin wave dispersion (lines) compared to experimental data from Fig. 4 in Ref. [18] (points). The parameters are defined as $\Gamma_{l\perp} = \frac{1}{2}([\Gamma_l]_{x,x} + [\Gamma_l]_{y,y})$ for $l = 1, 2, 3$. Values are given in meV. The small anisotropies $\Delta\Gamma_{l\perp} = \frac{1}{2}([\Gamma_l]_{x,x} - [\Gamma_l]_{y,y})$ and $\Delta\Gamma_{lz} = \Gamma_{l\perp} - \Gamma_{lz}$ are the same for all panels: $\Delta\Gamma_{1z}^{x/y} = \pm 0.65$ meV, $\Delta\Gamma_{1z}^{x/y} = 3.35$ meV, $\Delta\Gamma_{2\perp}^{a/b} = \pm 0.15$ meV, $\Delta\Gamma_{2z}^{a/b} = -0.65$ meV. (a) Theoretical exchange parameters obtained with $(U, J) = (3.2, 0.4)$ eV. (b)–(d) show results for different couplings in representative cases. The set used in (b) yields a good fitting of experiments. Special points: $X = (\pi, 0, 0)$, $M = (\pi, \pi, 0)$, $2X = (2\pi, 0, 0)$, $\Gamma = (0, 0, 0)$; lattice constants are set equal to 1 for simplicity.

Summarizing, by using a combination of LDA+SO+DMFT calculations and many-body perturbation theory, we derived the parameters of the superexchange Hamiltonian at second order. The results yield a Γ_1 comparable with experiments for, e.g., $(U, J) = (3.2, 0.4)$ eV or $(U, J) = (2.4, 0.0)$ eV; both set of parameters gives a similar insulating solution in LDA+SO+DMFT, with a half-filled effective j_{eff} state. Setting $J = 0$, however, yields isotropic exchange couplings, in contradiction with experiments. At the same time, we find that Γ_1 increases rapidly with J , everything else staying the same; thus Γ_1 is almost a factor of 2 too large for $(U, J) = (2.0, 0.4)$ eV. Furthermore, our calculations show that Γ_2 is antiferromagnetic and too small compared to the experimental estimate from spin wave spectra. This conclusion is very robust, i.e., it remains valid in the whole range of realistic values of the Hund's rule coupling and crystal-field integrals. Remarkably, although the spin-wave spectra are not sufficiently well described, the magnetic ordered structure stemming from the second-order couplings is in line with experiments. Experimentally, the magnetic structure has been determined by x-ray [53] and neutron diffraction [54]. The pseudospins form a canted antiferromagnetic structure in IrO_2 layers with the net magnetic moments projected along the b axis. The layer-stacking along c axis is of ABBA type and can be modified easily by a modest magnetic field (> 0.2 T) [21]. In the window of realistic screened Coulomb integrals, our findings are in line with these observations. Except for (unrealistically) large and negative $\varepsilon_{\text{CF}} \sim (-0.4, -0.3)$ eV, the condition $\alpha_{XY} > 0$ is always satisfied and therefore the

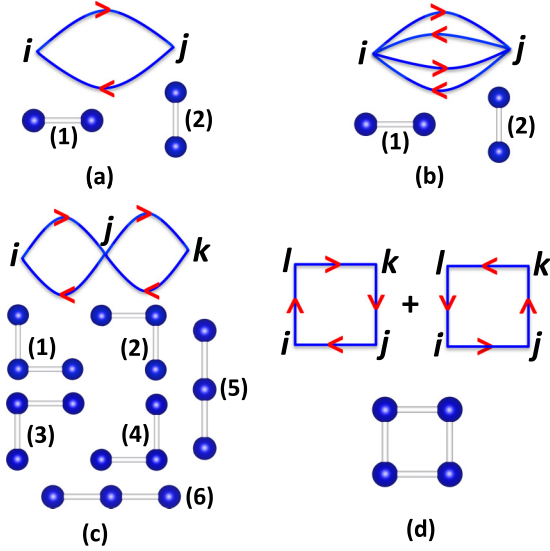


FIG. 6. Superexchange diagrams of second (a) and fourth order (the remaining ones). The latter split into processes involving two (b), three (c) and four sites (d). For each diagram, the possible site configurations are also shown; the terms are discussed in Appendix B.

magnetic moments lie in the IrO_2 layers. Finally, $\Gamma_z^{a/b} \sim 0$, indicating quite weak interlayer magnetic couplings.

Thus, on the one hand, the second-order Hamiltonian captures the main features for describing the ground state but, on the other hand, it is missing some essential ingredients for describing well, *alone*, the excited spectrum. In the light of these results, in the next section we analyze the effect of fourth-order terms.

B. Fourth-order terms

A possible solution to the discrepancies discussed above are higher-order superexchange terms, shown schematically in Fig. 6. In the case of La_2CuO_4 , it has been pointed out that a sizable ring exchange could explain the shape of spin waves [22,55–60], a fact taken often as an indication of a relatively weak Coulomb interaction. Also in the iridates, one could expect sizable fourth-order effects, as suggested, e.g., in Ref. [19]. Here we quantify their role.

The elements of the fourth-order many-body energy-gain matrix can be written as

$$\mathcal{M}_{g,g'}^{(4)} = \sum_{e'e''} \frac{\hat{H}_{ge}^T \hat{H}_{e'g'}^T \hat{H}_{g'e''}^T \hat{H}_{e''g'}^T}{\Delta E_e \Delta E_{e'}} \frac{1}{2} \left(\frac{1}{\Delta E_e} + \frac{1}{\Delta E_{e'}} \right) - \sum_{e'e''} \frac{\hat{H}_{ge}^T \hat{H}_{e'e''}^T \hat{H}_{e''g'}^T \hat{H}_{e'g'}^T}{\Delta E_e \Delta E_{e''} \Delta E_{e'}} \quad (22)$$

where $\Delta E_e = E_e^0 - E_g^0$, with E_g^0 and E_e^0 energies of ground (g) and excited (e) atomic states and \hat{H}^T is the hopping part of the Hamiltonian. Fourth-order terms from hopping integrals between nearest neighbors are sizably larger than those from longer range ones; thus we consider their effects only. The contributing processes can involve two, three, or four sites [61], as shown in Figs. 6(b)–6(d). For each diagram, we map

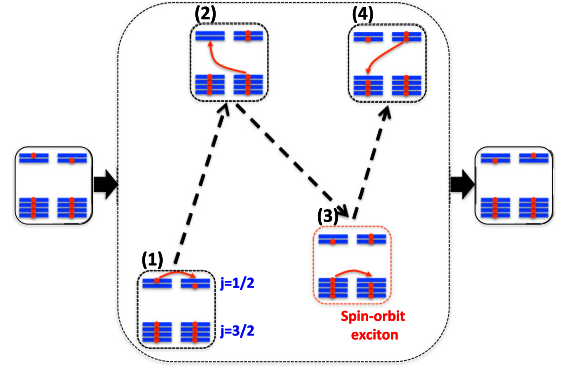


FIG. 7. The contribution of excitonic processes. The initial and final configurations have four electrons in the $j_{\text{eff}} = 3/2$ multiplet and one in the $j_{\text{eff}} = 1/2$ multiplet, both at site (i) and (i'). In the first step, a $j_{\text{eff}} = 1/2$ electron moves from site (i) to the empty $j_{\text{eff}} = 1/2$ state at the neighboring site (i'). In step (2), a $j_{\text{eff}} = 3/2$ electron from site (i') is transferred to the $j_{\text{eff}} = 1/2$ multiplet of site (i). The intermediate state is now a spin-orbit excitonic state. In step (3), an electron from site (i) in the $j_{\text{eff}} = 3/2$ multiplet moves to site (i') in the same multiplet. In step (4) a $j_{\text{eff}} = 1/2$ electron from site (i') moves back to site (i) but in the $j_{\text{eff}} = 3/2$ multiplet. This sequence of virtual excitations contributes to $\Gamma_1^{(b)}$.

the energy gain matrix $\mathcal{M}_{g,g'}^{(4)}$ into the effective pseudospin Hamiltonian as explained in Appendix B.

Compared to the case of the single-band half-filled Hubbard model, there are contributions from spin-orbit excitonic states via the term in the last line of Eq. (22); this is illustrated in Fig. 7 in a representative case. To quantify the role of excitonic processes, we perform calculations with and without such contributions. For diagrams in Fig. 6(b), the magnetic coupling matrix along x direction without excitonic terms is, for $U = 3.2$ eV,

$$\Gamma_{1x}^{(b)} = \begin{pmatrix} -2.1 & 0.0 & 0.0 \\ 0.0 & -2.1 & 0.0 \\ 0.0 & 0.0 & -2.1 \end{pmatrix} \text{meV}. \quad (23)$$

Adding the excitonic terms, we have

$$\Gamma_{1x}^{(b)} = \begin{pmatrix} 1.4 & 0.1 & 0.0 \\ -0.1 & 1.4 & 0.0 \\ 0.0 & 0.0 & 1.3 \end{pmatrix} \text{meV}. \quad (24)$$

For $U = 2.0$ eV, the matrices are instead

$$\Gamma_{1x}^{(b)} = \begin{pmatrix} -19.0 & 0.0 & 0.0 \\ 0.0 & -18.8 & 0.0 \\ 0.0 & 0.0 & -18.5 \end{pmatrix} \text{meV} \quad (25)$$

and

$$\Gamma_{1x}^{(b)} = \begin{pmatrix} -6.6 & 0.1 & 0.0 \\ -0.1 & -6.6 & 0.0 \\ 0.0 & 0.0 & -6.8 \end{pmatrix} \text{meV}. \quad (26)$$

The corresponding elements of $\Gamma_{1y}^{(b)}$ along the y direction can be obtained exchanging the first two diagonal elements of $\Gamma_{1x}^{(b)}$. These matrices show that accounting for excitonic processes reduces the value of the negative couplings on the diagonal and can even lead to a sign change. As a result, the

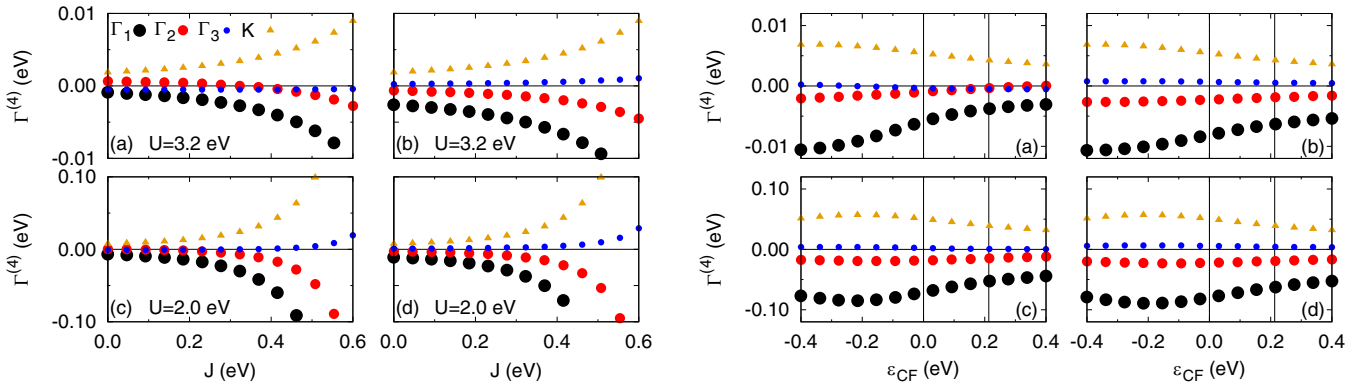


FIG. 8. The fourth-order exchange couplings as a function of Hund's rule coupling J (left panels) and crystal-field splitting (right panels). (a), (c) With excitonic states. (b), (d) Without excitonic states. (a), (b) $U = 3.2$ eV. (c), (d) $U = 2.0$ eV. The meaning of the symbols is the same for all panels.

contribution from the diagram in Fig. 6(b) is positive (antiferromagnetic) for $U = 3.2$ eV, while it remains ferromagnetic (negative) for smaller U . In the case of La_2CuO_4 , the corresponding parameter is ferromagnetic. Since Eqs. (25) and (26) show that the anisotropy is tiny, we will from now on neglect it. By collecting all the contributions from Figs. 6(b)–6(d), after taking the multiplicities on a square lattice into account, we finally have

$$\begin{aligned}
 \hat{H}_{\text{SE}}^{(4)} = & \frac{1}{2}(\Gamma_1^{(4)} + K^{(4)}) \sum_{\langle jj' \rangle_{\text{N}}} \tilde{\mathbf{S}}_j \cdot \tilde{\mathbf{S}}_{j'} \\
 & + \frac{1}{2} \left(\Gamma_2^{(4)} + \frac{1}{2} K^{(4)} \right) \sum_{\langle jj' \rangle_{\text{NN}}} \tilde{\mathbf{S}}_j \cdot \tilde{\mathbf{S}}_{j'} \\
 & + \frac{1}{2} \Gamma_3^{(4)} \sum_{\langle jj' \rangle_{\text{NNN}}} \tilde{\mathbf{S}}_j \cdot \tilde{\mathbf{S}}_{j'} \\
 & + 2K^{(4)} \sum_{\langle ijkl \rangle} ((\tilde{\mathbf{S}}_i \cdot \tilde{\mathbf{S}}_j)(\tilde{\mathbf{S}}_k \cdot \tilde{\mathbf{S}}_l) \\
 & + (\tilde{\mathbf{S}}_j \cdot \tilde{\mathbf{S}}_k)(\tilde{\mathbf{S}}_l \cdot \tilde{\mathbf{S}}_i) - (\tilde{\mathbf{S}}_i \cdot \tilde{\mathbf{S}}_k)(\tilde{\mathbf{S}}_j \cdot \tilde{\mathbf{S}}_l)). \quad (27)
 \end{aligned}$$

Here $\langle jj' \rangle_{\text{N}}$, $\langle jj' \rangle_{\text{NN}}$, and $\langle jj' \rangle_{\text{NNN}}$, indicate that the sum is over nearest (N), next-nearest (NN), and next-next-nearest (NNN) neighbors (both bonds counted), and $\langle ijkl \rangle$ on four spins on a plaquette (here each set of four spins is counted only once). The total effective exchange couplings obtained by fourth-order perturbation calculations for the representative values $(U, J) = (3.2, 0.4)$ eV and $(U, J) = (2.0, 0.4)$ eV are summarized in Table II. The small fourth-order DM term has been neglected.

Let us now discuss the results. First, the experimental magnetic ground state is still in line with the set of parameters obtained adding fourth-order terms. What about the spin-wave dispersion? The contributions from $K^{(4)}$ cancel out in linear spin-wave theory for the isotropic case [58]. Hence, only the remaining terms, $\Gamma_1^{(4)}$, $\Gamma_2^{(4)}$, and $\Gamma_3^{(4)}$, can be directly compared to values obtained fitting experimental magnon spectra. Table II shows that, once fourth-order terms are taken into account, a similar total $\Gamma_{\text{tot}}^{(1)}$ is obtained for $U = 3.2$ eV and $U = 2.0$ eV, due to cancellation of terms. This shows that it is hard to distinguish the two modelizations by compar-

ing to spin-wave spectra, at least if one looks to the largest couplings only. Things are different for $\Gamma_{\text{tot}}^{(2)}$; for $U = 2.0$ eV, the fourth-order term offsets the second-order one, making the total effective $\Gamma_{\text{tot}}^{(2)}$ not only ferromagnetic but also of the right order of magnitude.

To study the stability of this conclusion, in Fig. 8, we investigate the effects of U , J , and ε_{CF} on the total fourth-order couplings $\Gamma_1^{(4)}$, $\Gamma_2^{(4)}$, $\Gamma_3^{(4)}$, and $K^{(4)}$. By comparing the top and bottom panels, one sees that, as expected, the fourth-order couplings increase by almost an order of magnitude with decreasing U from 3.2 to 2.0 eV, everything else staying the same. The effects of the Hund's rule coupling J are much less trivial; increasing J makes $\Gamma_1^{(4)}$ more negative, everything else staying the same, partially compensating the increase found in the corresponding antiferromagnetic second-order term, shown in Fig. 3. Thus, the total $\Gamma_{\text{tot}}^{(1)}$ is less sensitive to the exact value of J than the two components (second and fourth order) alone. For example, for $U = 2.0$ eV, if $J = 0.2$ eV we obtain $\Gamma_1^{(4)} \sim -20$ meV, and $\Gamma_{\text{tot}}^{(1)} \sim 78$ meV, while for $J = 0.4$ eV we find $\Gamma_1^{(4)} \sim -55$ meV and $\Gamma_{\text{tot}}^{(1)} \sim 72$ meV. The situation is very different for $\Gamma_{\text{tot}}^{(2)}$, since at second order this parameter is 1 meV or smaller. Thus, $\Gamma_2^{(4)}$ can dominate if J is sufficiently large; indeed, for $J \sim 0.4$ eV we find $\Gamma_2^{(4)} \sim -16$ meV. This yields good agreement with experiments. It has to be said, however, that the value of $\Gamma_2^{(4)}$ quickly drops, reducing J , and for $J = 0.2$ eV it is already merely $\Gamma_2^{(4)} \sim -2.5$ meV. This can be seen in Fig. 8(c). The figure also shows that increasing the crystal-field splitting has the largest effect for $\Gamma_1^{(4)}$ and $K^{(4)}$; the more positive the crystal field is, the smaller (in absolute value) the two parameters are. Instead, for $\Gamma_2^{(4)}$, the effect is weak. Finally, for all realistic parameter values, $\Gamma_3^{(4)}$ is very small.

The total magnetic couplings are shown in Fig. 9. The figure shows that the main parameter, $\Gamma_{\text{tot}}^{(1)}$ has a value close to experiments (assuming $\approx 60 \pm 10$ meV) in a reasonable range of Coulomb parameters, e.g., $U \sim 2.5$ eV and $J \sim 0.3$ eV. For $\Gamma_{\text{tot}}^{(2)}$, instead, a value comparable to the one extracted from experimental spin-wave spectra is only obtained if U is sufficiently small and J sufficiently large. The crystal-field splitting variation (within a realistic interval) appears less crucial.

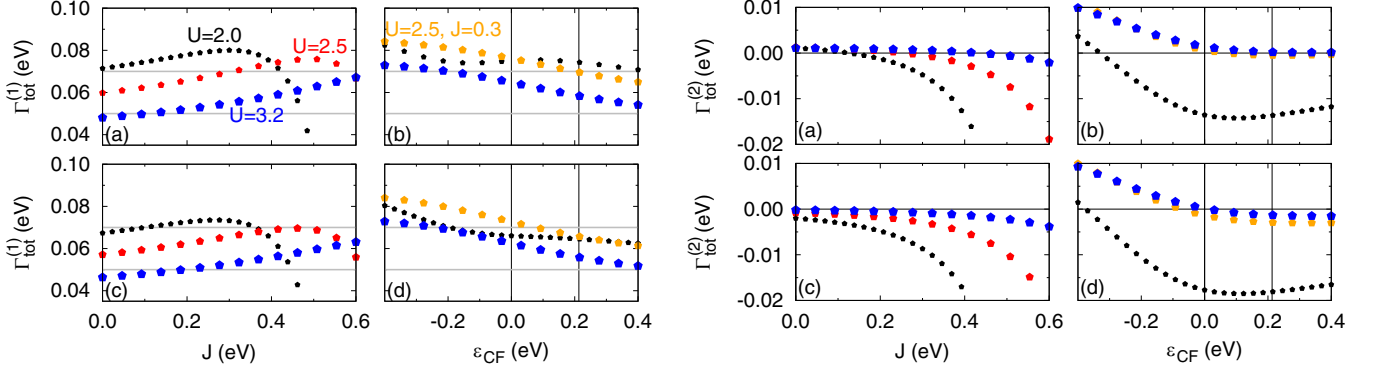


FIG. 9. Total couplings $\Gamma_{\text{tot}}^{(1)}$ (left) and $\Gamma_{\text{tot}}^{(2)}$ (right) as a function of J and ε_{CF} . (b), (d) Results for three couples of (U, J) values, $(3.2, 0.4)$, $(2.5, 0.3)$, $(2.0, 0.4)$, all in eV. (a), (b) With excitonic processes. (c), (d) No excitonic processes. Straight lines: Interval of ± 10 meV around the experimental value $\Gamma_1 \sim 60$ meV.

III. DISCUSSION AND CONCLUSION

We performed LDA+SO+DMFT calculations for Sr_2IrO_4 in the paramagnetic phase. Our results show that, in line with previous theoretical and experimental works, the system is strongly correlated but not far from the Mott transition, and it is characterized by a half-filled $j_{\text{eff}} = 1/2$ multiplet. This indicates that the magnetic couplings can be obtained in the effective $j_{\text{eff}} = 1/2$ pseudospin picture via a strong coupling expansion. At the same time, however, these results point to a possible important role of fourth-order terms. We thus calculated the magnetic couplings by many-body perturbation theory up to fourth order.

We studied the superexchange tensors obtained as a function of the screened Coulomb integrals, (U, J) , and the crystal-field splitting ε_{CF} . We find that the nearest-neighbor coupling, $\Gamma_{\text{tot}}^{(1)}$ is in reasonable agreement with experiments for realistic choices of (U, J) . Its microscopic origin, however, changes rapidly with increasing U and J , even staying within the window of realistic values. More specifically, for $U \sim 3.2$ eV or larger, it is dominated by second-order terms; instead, for $U \sim 2.0$ eV, fourth-order contributions can be sizable and even partially compensate second-order ones if J is sufficiently large. The situation is different for the next-nearest-neighbor coupling, $\Gamma_{\text{tot}}^{(2)}$. At second order, the latter is always too small with respect to experimental estimates; furthermore, it has the wrong sign. Adding fourth order terms can change the sign of $\Gamma_{\text{tot}}^{(2)}$, however, making it ferromagnetic; for $U \sim 2.0$ eV and $J \sim 0.4$ eV, the value of $\Gamma_{\text{tot}}^{(2)}$ is close to the experimental estimate. We have also shown that spin-orbit excitonic states play a key role at fourth order and reduce the absolute value of $\Gamma_{\text{tot}}^{(2)}$. Finally, our calculations show that, in the full range of realistic parameters, the next-next-nearest-neighbor superexchange coupling, $\Gamma_{\text{tot}}^{(3)}$, is too small with respect to the value needed to fit spin-wave dispersions using linear spin-wave theory.

Thus, for (U, J) values that give, in LDA+SO+DMFT calculations, a Mott insulating state with half-filled $j_{\text{eff}} = 1/2$ state, second-order superexchange terms dominate, despite the small gap, as in the truly strong-coupling limit. This is what happens, for example, for $(U, J) = (3.2, 0.4)$ eV, $(U, J) = (2.5, 0.3)$ eV, or $(U, J) = (2.4, 0.0)$ eV, all values used in the literature (and yielding a small but finite

Mott gap), corresponding to an average Coulomb interaction $U_{\text{avg}} = 1.9 - 2.4$ eV. The reason is that, depending on the case, either U is too large or J too small—or both at the same time—for sizable fourth-order contributions. In this situation, a ferromagnetic $\Gamma_2 \sim -15$ meV and $\Gamma_3 \sim |\Gamma_2|$ are hard to explain within superexchange theory alone, at least when starting from the t_{2g} Hubbard model Eq. (1). The discrepancies would suggest that the microscopic model should be expanded to explicitly include more degrees of freedom as well as the ferromagnetic Coulomb exchange.

Since in Sr_2IrO_4 the experimental gap is small, about 0.1–0.6 eV [27–33], and LDA+SO+DMFT calculations give a Mott gap in line with these data for $U_{\text{avg}} \sim 2.4$ eV, it is still possible that a different scenario occurs, however. DMFT results are based on the local self-energy approximation; going to large clusters remains very challenging, in particular, in the presence of spin-orbit interaction. If nonlocal correlation effects were taken into account, however, the gap could already open for a slightly smaller U_{avg} , not far from the cRPA estimate. Alternatively, in the paramagnetic phase, Sr_2IrO_4 could even remain a bad metal with very heavy masses, becoming an insulator only below the magnetic transition [25,34,35]. In these circumstances, true signatures of the intermediate-coupling regime could appear. In fact, should the Hund's rule J be large enough ($J \sim 0.4$ for $U = 2.0$ eV), fourth-order terms could explain a ferromagnetic Γ_2 (alone or in combination with Coulomb exchange). In addition, as has been shown for the single-band Hubbard model on a square lattice, quantum fluctuations could justify the suppression of the excitation energy at the X point, without the need of a large Γ_3 [19,59,60]; this is true, in particular, if the ratio $r_R = 2K/(\Gamma_{\text{tot}}^{(1)} + K)$ is as large as $r_R \sim 0.7$, the value we obtain for $(U, J) = (2.0, 0.4)$ eV.

In conclusion, we have identified two possible scenarios. In the first, despite the small charge gap, the magnetic couplings are dominated by second-order terms, as in the strong coupling regime. In this case, the dominant coupling, Γ_1 , is well described by standard superexchange theory within the three-band t_{2g} Hubbard model. For explaining the sign and size of the long-range Γ_2 and Γ_3 couplings, however, terms beyond t_{2g} superexchange interactions have to be considered. In the second scenario, instead, true intermediate-coupling effects play an important role. In this regime, if J is sufficiently

TABLE III. The t_{2g}^5 multiplets in the presence of crystal field and spin-orbit coupling, with Coulomb energy $E_U = 10U - 20J$, in the one-electron basis which yields the local Hamiltonian Eq. (3). The states are defined as $|M^h\rangle_\sigma = c_{M\sigma}^\dagger c_{M_2\uparrow}^\dagger c_{M_2\downarrow}^\dagger c_{M_1\uparrow}^\dagger c_{M_1\downarrow}^\dagger |0\rangle$. We use the same notations of Ref. [51]. The coefficients α_5 and α_6 are positive.

$ N; \alpha\rangle$	$E = E_{\text{atom}} - E_U$
$ 5; \Gamma_6, \sigma\rangle = -\frac{1}{\sqrt{2}}(XZ^h\rangle_\sigma - 2i\sigma YZ^h\rangle_\sigma)$	$3\epsilon_{\text{CF}} + \frac{\lambda_X}{2}$
$ 5; \Gamma_7'', \sigma\rangle = -i\alpha_5 XY^h\rangle_\sigma - \frac{\alpha_6}{\sqrt{2}}(XZ^h\rangle_{-\sigma} - 2i\sigma YZ^h\rangle_{-\sigma})$	$4\epsilon_{\text{CF}} + \frac{1}{2}(-\epsilon_{\text{CF}} - \frac{\lambda_Z}{2} + \sqrt{(\epsilon_{\text{CF}} + \frac{\lambda_Z}{2})^2 + 2\lambda_{X/Y}^2})$
$ 5; \Gamma_7', \sigma\rangle = +i\alpha_6 XY^h\rangle_\sigma - \frac{\alpha_5}{\sqrt{2}}(XZ^h\rangle_{-\sigma} - 2i\sigma YZ^h\rangle_{-\sigma})$	$4\epsilon_{\text{CF}} + \frac{1}{2}(-\epsilon_{\text{CF}} - \frac{\lambda_Z}{2} - \sqrt{(\epsilon_{\text{CF}} + \frac{\lambda_Z}{2})^2 + 2\lambda_{X/Y}^2})$
$\alpha_5^2 = \frac{2\lambda_{X/Y}^2}{(\epsilon_{\text{CF}} + \frac{\lambda_Z}{2} - \sqrt{(\epsilon_{\text{CF}} + \frac{\lambda_Z}{2})^2 + 2\lambda_{X/Y}^2})^2 + 2\lambda_{X/Y}^2}, \quad \alpha_5^2 + \alpha_6^2 = 1.$	

large, a ferromagnetic Γ_2 can already be obtained from t_{2g} superexchange theory. Ultimately, the independent experimental determination of K remains the smoking gun for identifying the correct picture. In the case of La_2CuO_4 , evidence in favor of a sizable K was gathered via the temperature dependence of the static susceptibility at high temperature [58], although the question is far from settled. Experiments with similar goals could help shed light on the correct modelization for Sr_2IrO_4 . This could also help in understanding the behavior of other systems, such as the bilayer $\text{Sr}_3\text{Ir}_2\text{O}_7$, for which long-range couplings have also been used to fit the RIXS spin-wave dispersion [62].

ACKNOWLEDGMENTS

G.Z. acknowledges financial support by the National Natural Science Foundation of China under Grants No. 12074384 and No. 11774349. The authors gratefully acknowledge the Gauss Centre for Supercomputing e.V. [63] for funding this project by providing computing time on the GCS Supercomputer JUWELS at Jülich Supercomputing Centre (J.S.C.). The authors also acknowledge computing time granted through JARA on the supercomputers JURECA, which was very important for code development and extension.

APPENDIX A: THE t_{2g}^5 MULTIPLTS IN ATOMIC LIMIT

The multiplets for t_{2g}^5 configuration with both tetragonal crystal-field and spin-orbit coupling are listed in Table III. The lowest energy doublet $|5; \Gamma_7', \sigma\rangle$ is redefined as pseudospin states $|\sigma\rangle$ in the main text.

APPENDIX B: DERIVATION OF FOURTH-ORDER TERMS

In this Appendix, we explain how we calculate the contributions of the diagrams in Fig. 6. For Fig. 6(b), involving only two sites, we simply use Eq. (7), replacing $\mathcal{M}^{(2)}$ with $\mathcal{M}^{(4)}$. For the multisite diagrams Figs. 6(c) and 6(d), we ignore the tiny anisotropy and adopt Dirac's approach [58,64,65]. As an intermediate step, we thus map the interaction into

$$\mathcal{H}_{\text{SE}}^{(c/d)} = -\frac{1}{2} \sum_{\xi} (-1)^{p_{\xi}} \Gamma_{\xi}^{(c/d)} \mathcal{P}_{\xi}^{\sigma}, \quad (\text{B1})$$

where Γ_{ξ} is the exchange parameter and $\mathcal{P}_{\xi}^{\sigma}$ are the cyclic spin permutation operators

$$\mathcal{P}_{123\dots N}^{\sigma} |\sigma_1, \sigma_2, \sigma_3, \dots, \sigma_N\rangle = |\sigma_N, \sigma_1, \sigma_2, \dots, \sigma_{N-1}\rangle.$$

In Eq. (B1), p_{ξ} is even (odd) for an odd (even) number of pseudospins. Thus, if $\Gamma_{\xi}^{(c/d)} > 0$, cyclic permutations with an odd number of pseudospins result in a ferromagnetic exchange [66]. For $N = 2$, we have

$$\mathcal{P}_{ij}^{\sigma} = \frac{1}{2}(1 + \vec{\sigma}_i \cdot \vec{\sigma}_j), \quad (\text{B2})$$

where $\vec{\sigma}_i$ and $\vec{\sigma}_j$ are Pauli matrices. Since for $N > 2$,

$$\mathcal{P}_{123\dots N}^{\sigma} = \mathcal{P}_{12}^{\sigma} \mathcal{P}_{23}^{\sigma} \dots \mathcal{P}_{N-1,N}^{\sigma}, \quad (\text{B3})$$

for three and four spins, we have $\mathcal{P}_{ijk}^{\sigma} = \mathcal{P}_{ij}^{\sigma} \mathcal{P}_{jk}^{\sigma}$ and $\mathcal{P}_{ijkl}^{\sigma} = \mathcal{P}_{ij}^{\sigma} \mathcal{P}_{jk}^{\sigma} \mathcal{P}_{kl}^{\sigma}$. Given that the inverse of $\mathcal{P}_{\xi}^{\sigma}$ equals its complex conjugate, the two relevant terms at fourth order can then be expressed as

$$\begin{aligned} \mathcal{P}_{ijk}^{\sigma} + (\mathcal{P}_{ijk}^{\sigma})^{-1} &= \frac{1}{2}(1 + \vec{\sigma}_i \cdot \vec{\sigma}_j + \vec{\sigma}_j \cdot \vec{\sigma}_k + \vec{\sigma}_k \cdot \vec{\sigma}_i) \\ &= \mathcal{P}_{ij}^{\sigma} + \mathcal{P}_{jk}^{\sigma} + \mathcal{P}_{ki}^{\sigma} - 1 \end{aligned} \quad (\text{B4})$$

and

$$\mathcal{P}_{ijkl}^{\sigma} + (\mathcal{P}_{ijkl}^{\sigma})^{-1} = -1 + \mathcal{P}_{ik}^{\sigma} + \mathcal{P}_{jl}^{\sigma} + \mathcal{P}_{ij}^{\sigma} \mathcal{P}_{kl}^{\sigma} + \mathcal{P}_{jk}^{\sigma} \mathcal{P}_{li}^{\sigma} - \mathcal{P}_{ik}^{\sigma} \mathcal{P}_{jl}^{\sigma}. \quad (\text{B5})$$

For Fig. 6(c), we thus obtain the following exchange terms for three sites, ordered as i, j, k :

$$\begin{aligned} \mathcal{H}_{\text{SE}}^{(c)} &= \frac{1}{2}(\Gamma_{1;B}^{(c)} + \Gamma_{1;L}^{(c)})(\mathcal{P}_{ij}^{\sigma} + \mathcal{P}_{jk}^{\sigma}) + \frac{1}{2}(\Gamma_{2;B}^{(c)} + \Gamma_{3;L}^{(c)})\mathcal{P}_{ik}^{\sigma} \\ &\quad - \frac{1}{2}(\Gamma_{\mathcal{T}B}^{(c)} + \Gamma_{\mathcal{T}L}^{(c)})(\mathcal{P}_{ijk}^{\sigma} + (\mathcal{P}_{ijk}^{\sigma})^{-1}). \end{aligned}$$

The possible site configurations (which we label with X) contributing are shown in Fig. 6. The bent configurations, (1)–(4) are indicated as $X=B$, while the linear configurations, (5) and (6), as $X=L$. The couplings $\Gamma_{l;X}^{(c)}$ contribute to $\Gamma_l^{(4)}$ only, where $l = 1, 2, 3$ indicates if the sites are first, second, or third neighbors. The coupling $\Gamma_{\mathcal{T}X}^{(c)}$ with $X=B$ contributes to both $\Gamma_1^{(4)}$ and $\Gamma_2^{(4)}$, with values $\Gamma_{1;\mathcal{T}B}^{(c)} = \Gamma_{2;\mathcal{T}B}^{(c)} = -\Gamma_{\mathcal{T}B}^{(c)}$; instead, for $X=L$ the contributions are $\Gamma_{1;\mathcal{T}L}^{(c)} = \Gamma_{3;\mathcal{T}L}^{(c)} = -\Gamma_{\mathcal{T}L}^{(c)}$. In Table IV, we give the final results for $(U, J) = (3.2, 0.4)$ eV and $(U, J) = (2.0, 0.4)$ eV. The table evidences once more that the numerical values of the exchange couplings can vary sizably, including excitonic processes, a peculiarity of iridates with respect to cuprates. In

TABLE IV. Exchange couplings (in meV) from fourth-order diagrams (b)–(d). Hopping parameters are obtained via LDA+SO calculations. Coulomb parameters: $U = 3.2$ eV (left), $U = 2.0$ eV (right), $J = 0.4$ eV. Superscripts (b)–(d) indicate the diagrams from which the parameter originates; diagrams and associated possible site configurations are illustrated in Fig. 6. Notice that $\Gamma_{1;TB}^{(c)} = \Gamma_{2;TB}^{(c)} = -\Gamma_{TB}^{(c)}$, $\Gamma_{1;TL}^{(c)} = \Gamma_{3;TL}^{(c)} = -\Gamma_{TL}^{(c)}$, and $\Gamma_{1;\mathcal{T}}^{(d)} = \Gamma_{2;\mathcal{T}}^{(d)} = -\Gamma_{\mathcal{T}}^{(d)}$ by construction; here B stands for bent [diagram (c), configurations (1)–(4)], L for linear [diagram (c), configurations (5) and (6)], P for plaquette (diagram (d)). In addition \mathcal{T} stands for (ijk) and S for $(ijkl)$.

Type	$U = 3.2$ eV				No excitons				$U = 2.0$ eV				No excitons					
(b)	$\Gamma_{1x}^{(b)} = \begin{pmatrix} 1.4 & 0.1 & 0.0 \\ -0.1 & 1.4 & 0.0 \\ 0.0 & 0.0 & 1.3 \end{pmatrix}$				$\begin{pmatrix} -2.1 & 0.0 & 0.0 \\ 0.0 & -2.1 & 0.0 \\ 0.0 & 0.0 & -2.1 \end{pmatrix}$				$\begin{pmatrix} -6.6 & 0.1 & 0.0 \\ -0.1 & -6.6 & 0.0 \\ 0.0 & 0.0 & -6.8 \end{pmatrix}$				$\begin{pmatrix} -19.0 & 0.0 & 0.0 \\ 0.0 & -18.8 & 0.0 \\ 0.0 & 0.0 & -18.5 \end{pmatrix}$					
	conf	\mathcal{P}	Γ_1	Γ_2	Γ_3	K	Γ_1	Γ_2	Γ_3	K	Γ_1	Γ_2	Γ_3	K	Γ_1	Γ_2	Γ_3	K
	B	ij	-0.9	-0.7			-0.7	-0.4			-6.5	0.2			-6.0	-3.2		
(c)	L	ij	-0.4		-1.7		-0.6		-0.2		-4.0		-6.1		-5.0		-1.2	
	B	$\mathcal{T} : ijk$	+0.4	+0.4			+0.8	+0.8			+5.1	+5.1			+6.2	+6.2		
	L	$\mathcal{T} : ijk$	+1.2		+1.2		+0.7		+0.7		+7.0		+7.0		+5.7		+5.7	
	conf	\mathcal{P}	Γ_1	Γ_2	Γ_3	K					Γ_1	Γ_2	Γ_3	K				
(d)	P	ij	+0.7	+0.4							+7.1	+5.2						
	P	$\mathcal{T} : ijk$	-1.3	-1.3							-15.6	-15.6						
	P	$S : ijkl$				+4.3									+40.2			

addition, the table shows that \mathcal{T} couplings from Fig. 6(c) are all antiferromagnetic and can compensate the ferromagnetic contributions from other diagrams.

Figure 6(d) involves four sites, ordered as i, j, k, l . The associated SU(2)-symmetric terms can be expressed as

$$\begin{aligned}
\mathcal{H}_{SE}^{(d)} = & \frac{\Gamma_1^{(d)}}{2} (\mathcal{P}_{ij}^\sigma + \mathcal{P}_{jk}^\sigma + \mathcal{P}_{kl}^\sigma + \mathcal{P}_{li}^\sigma) + \frac{\Gamma_2^{(d)}}{2} (\mathcal{P}_{ik}^\sigma + \mathcal{P}_{jl}^\sigma) \\
& - \frac{\Gamma_{\mathcal{T}}^{(d)}}{2} (\mathcal{P}_{ijk}^\sigma + (\mathcal{P}_{ijk}^\sigma)^{-1} + \mathcal{P}_{ikl}^\sigma + (\mathcal{P}_{ikl}^\sigma)^{-1}) \\
& + \mathcal{P}_{ijl}^\sigma + (\mathcal{P}_{ijl}^\sigma)^{-1} + \mathcal{P}_{jkl}^\sigma + (\mathcal{P}_{jkl}^\sigma)^{-1} \\
& + \frac{K_S^{(d)}}{2} (\mathcal{P}_{ijkl}^\sigma + (\mathcal{P}_{ijkl}^\sigma)^{-1}). \quad (B6)
\end{aligned}$$

Spin-orbit excitonic states do not contribute. The coupling $\Gamma_{\mathcal{T}}^{(d)}$ contributes to both $\Gamma_1^{(4)}$ and $\Gamma_2^{(4)}$ with values $\Gamma_{1;\mathcal{T}}^{(d)} = \Gamma_{2;\mathcal{T}}^{(d)} = -\Gamma_{\mathcal{T}}^{(d)}$. The numerical values obtained are listed in Table IV; the \mathcal{T} couplings are all ferromagnetic.

Finally, collecting all the contributions

$$\begin{aligned}
\hat{H}_{SE}^{(4)} = & \frac{1}{2} (\Gamma_1^{(4)} + K^{(4)}) \sum_{\langle jj' \rangle_N} \tilde{\mathbf{S}}_j \cdot \tilde{\mathbf{S}}_{j'} \\
& + \frac{1}{2} \left(\Gamma_2^{(4)} + \frac{1}{2} K^{(4)} \right) \sum_{\langle jj' \rangle_{NN}} \tilde{\mathbf{S}}_j \cdot \tilde{\mathbf{S}}_{j'}
\end{aligned}$$

$$\begin{aligned}
& + \frac{1}{2} \Gamma_3^{(4)} \sum_{\langle jj' \rangle_{NNN}} \tilde{\mathbf{S}}_j \cdot \tilde{\mathbf{S}}_{j'} \\
& + 2K^{(4)} \sum_{\langle ijkl \rangle} ((\tilde{\mathbf{S}}_i \cdot \tilde{\mathbf{S}}_j)(\tilde{\mathbf{S}}_k \cdot \tilde{\mathbf{S}}_l) \\
& + (\tilde{\mathbf{S}}_j \cdot \tilde{\mathbf{S}}_k)(\tilde{\mathbf{S}}_l \cdot \tilde{\mathbf{S}}_i) - (\tilde{\mathbf{S}}_i \cdot \tilde{\mathbf{S}}_k)(\tilde{\mathbf{S}}_j \cdot \tilde{\mathbf{S}}_l)), \quad (B7)
\end{aligned}$$

where we took also the multiplicities on a square lattice into account. Here $\langle jj' \rangle_N$, $\langle jj' \rangle_{NN}$, and $\langle jj' \rangle_{NNN}$, indicate that the sum is over nearest (N), next nearest (NN), and next-next nearest (NNN) neighbors (both bonds counted), and $\langle ijkl \rangle$ on four spins on a plaquette (here each set of four spins is counted only once). The small fourth-order DM term has been neglected. The total fourth-order parameters are given by

$$\begin{aligned}
\Gamma_1^{(4)} = & \frac{1}{3} \text{Tr}[\Gamma_{1x}^{(b)}] + 4\Gamma_{1;B}^{(c)} + 2\Gamma_{1;L}^{(c)} + 4\Gamma_{1;TB}^{(c)} + 2\Gamma_{1;TL}^{(c)} \\
& + 2\Gamma_1^{(d)} + 4\Gamma_{1;\mathcal{T}}^{(d)}, \quad (B8)
\end{aligned}$$

$$\Gamma_2^{(4)} = 2\Gamma_{2;B}^{(c)} + 2\Gamma_{2;TB}^{(c)} + \Gamma_2^{(d)} + 2\Gamma_{2;\mathcal{T}}^{(d)} \quad (B9)$$

$$\Gamma_3^{(4)} = \Gamma_{3;L}^{(c)} + \Gamma_{3;TL}^{(c)} \quad (B9)$$

$$K^{(4)} = K_S^{(d)}. \quad (B10)$$

The total effective exchange couplings obtained by fourth-order perturbation calculations for the representative values $(U, J) = (3.2, 0.4)$ eV and $(U, J) = (2.0, 0.4)$ eV are summarized in Table II.

- [1] F. Wang and T. Senthil, *Phys. Rev. Lett.* **106**, 136402 (2011).
[2] H. Watanabe, T. Shirakawa, and S. Yunoki, *Phys. Rev. Lett.* **110**, 027002 (2013).
[3] Z. Y. Meng, Y. B. Kim, and H. Y. Kee, *Phys. Rev. Lett.* **113**, 177003 (2014).

- [4] Y. K. Kim, O. Krupin, J. D. Denlinger, A. Bostwick, E. Rotenberg, Q. Zhao, J. F. Mitchell, J. W. Allen, and B. J. Kim, *Science* **345**, 187 (2014).
[5] A. de la Torre, S. McKeown Walker, F. Y. Bruno, S. Ricco, Z. Wang, I. Gutierrez Lezama, G. Scheerer, G. Giriat, D. Jaccard,

- C. Berthod, T. K. Kim, M. Hoesch, E. C. Hunter, R. S. Perry, A. Tamai, and F. Baumberger, *Phys. Rev. Lett.* **115**, 176402 (2015).
- [6] Y. K. Kim, N. H. Sung, J. D. Denlinger, and B. J. Kim, *Nat. Phys.* **12**, 37 (2016).
- [7] Y. Cao, Q. Wang, J. A. Waugh, T. J. Reber, H. Li, X. Zhou, S. Parham, S.-R. Park, N. C. Plumb, E. Rotenberg, A. Bostwick, J. D. Denlinger, T. Qi, M. A. Hermele, G. Cao, and D. S. Dessau, *Nat. Commun.* **7**, 11367 (2016).
- [8] Y. Hu, X. Chen, S.-T. Peng, C. Lane, M. Matzelle, Z.-L. Sun, M. Hashimoto, D.-H. Lu, E. F. Schwier, M. Arita, T. Wu, R. S. Markiewicz, K. Shimada, X.-H. Chen, Z.-X. Shen, A. Bansil, S. D. Wilson, and J.-F. He, *Phys. Rev. Lett.* **123**, 216402 (2019).
- [9] S. Boseggia, R. Springell, H. C. Walker, H. M. Rønnow, Ch. Rüegg, H. Okabe, M. Isobe, R. S. Perry, S. P. Collins, and D. F. McMorrow, *Phys. Rev. Lett.* **110**, 117207 (2013).
- [10] G. Jackeli and G. Khaliullin, *Phys. Rev. Lett.* **102**, 017205 (2009). Our results reduce to those of this paper if we adopt the same approximations. To compare Eq. (5) to our results, set $\vec{J} = [\Gamma_1]_{\perp}$.
- [11] B. H. Kim, G. Khaliullin, and B. I. Min, *Phys. Rev. Lett.* **109**, 167205 (2012).
- [12] S. Fujiyama, H. Ohsumi, T. Komesu, J. Matsuno, B. J. Kim, M. Takata, T. Arima, and H. Takagi, *Phys. Rev. Lett.* **108**, 247212 (2012).
- [13] N. A. Bogdanov, V. M. Katukuri, J. Romhányi, V. Yushankhai, V. Kataev, B. Büchner, J. van den Brink, and L. Hozoi, *Nat. Commun.* **6**, 7306 (2015). In this paper, $\Gamma_1 \sim 48$ meV was obtained for the nearest-neighbor exchanges.
- [14] V. M. Katukuri, H. Stoll, J. van den Brink, and L. Hozoi, *Phys. Rev. B* **85**, 220402(R) (2012). In this work the value $\Gamma_1 \sim 51$ meV was obtained for the nearest-neighbor exchange, taking spin-orbit coupling into account.
- [15] J. Kim, D. Casa, M. H. Upton, T. Gog, Y.-J. Kim, J. F. Mitchell, M. van Veenendaal, M. Daghofer, J. van den Brink, G. Khaliullin, and B. J. Kim, *Phys. Rev. Lett.* **108**, 177003 (2012).
- [16] I. V. Solovyev, V. V. Mazurenko, and A. A. Katanin, *Phys. Rev. B* **92**, 235109 (2015).
- [17] J. G. Vale, S. Boseggia, H. C. Walker, R. Springell, Z. Feng, E. C. Hunter, R. S. Perry, D. Prabhakaran, A. T. Boothroyd, S. P. Collins, H. M. Rønnow, and D. F. McMorrow, *Phys. Rev. B* **92**, 020406(R) (2015).
- [18] D. Pincini, J. G. Vale, C. Donnerer, A. de la Torre, E. C. Hunter, R. Perry, M. Moretti Sala, F. Baumberger, and D. F. McMorrow, *Phys. Rev. B* **96**, 075162 (2017).
- [19] K. Misumi, K. Seki, and Y. Ohta, *JPS Conf. Proc.* **3**, 014021 (2014).
- [20] B. Keimer, R. J. Birgeneau, A. Cassanho, Y. Endoh, M. Greven, M. A. Kastner, and G. Shirane, *Z. Phys. B* **91**, 373 (1993).
- [21] D. Haskel, G. Fabbris, J. H. Kim, L. S. I. Veiga, J. R. L. Mardegan, C. A. Escanhoela, Jr., S. Chikara, V. Struzhkin, T. Senthil, B. J. Kim, G. Cao, and J.-W. Kim, *Phys. Rev. Lett.* **124**, 067201 (2020).
- [22] R. Coldea, S. M. Hayden, G. Aeppli, T. G. Perring, C. D. Frost, T. E. Mason, S.-W. Cheong, and Z. Fisk, *Phys. Rev. Lett.* **86**, 5377 (2001).
- [23] G. Zhang and E. Pavarini, *Phys. Rev. B* **101**, 205128 (2020).
- [24] C. Martins, M. Aichhorn, L. Vaugier, and S. Biermann, *Phys. Rev. Lett.* **107**, 266404 (2011).
- [25] R. Arita, J. Kuneš, A. V. Kozhevnikov, A. G. Eguiluz, and M. Imada, *Phys. Rev. Lett.* **108**, 086403 (2012).
- [26] C. Martins, M. Aichhorn, and S. Biermann, *J. Phys.: Condens. Matter.* **29**, 263001 (2017).
- [27] B. J. Kim, H. Jin, S. J. Moon, J.-Y. Kim, B.-G. Park, C. S. Leem, J. Yu, T. W. Noh, C. Kim, S.-J. Oh, J.-H. Park, V. Durairaj, G. Cao, and E. Rotenberg, *Phys. Rev. Lett.* **101**, 076402 (2008).
- [28] S. J. Moon, Hosub Jin, W. S. Choi, J. S. Lee, S. S. A. Seo, J. Yu, G. Cao, T. W. Noh, and Y. S. Lee, *Phys. Rev. B* **80**, 195110 (2009).
- [29] K. Ishii, I. Jarrige, M. Yoshida, K. Ikeuchi, J. Mizuki, K. Ohashi, T. Takayama, J. Matsuno, and H. Takagi, *Phys. Rev. B* **83**, 115121 (2011).
- [30] D. Haskel, G. Fabbris, M. Zhernenkov, P. P. Kong, C. Q. Jin, G. Cao, and M. van Veenendaal, *Phys. Rev. Lett.* **109**, 027204 (2012).
- [31] J. Dai, E. Calleja, G. Cao, and K. McElroy, *Phys. Rev. B* **90**, 041102(R) (2014).
- [32] Q. Wang, Y. Cao, J. A. Waugh, S. R. Park, T. F. Qi, O. B. Korneta, G. Cao, and D. S. Dessau, *Phys. Rev. B* **87**, 245109 (2013).
- [33] K. Wang, N. Bachar, J. Teyssier, W. Luo, C. W. Rischau, G. Scheerer, A. de la Torre, R. S. Perry, F. Baumberger, and D. van der Marel, *Phys. Rev. B* **98**, 045107 (2018).
- [34] D. Hsieh, F. Mahmood, D. H. Torchinsky, G. Cao, and N. Gedik, *Phys. Rev. B* **86**, 035128 (2012).
- [35] A. Yamasaki, S. Tachibana, H. Fujiwara, A. Higashiyama, A. Irizawa, O. Kirilmaz, F. Pfaff, P. Scheiderer, J. Gabel, M. Sing, T. Muro, M. Yabashi, K. Tamasaku, H. Sato, H. Namatame, M. Taniguchi, A. Hloskovskyy, H. Yoshida, H. Okabe, and M. Isobe, *Phys. Rev. B* **89**, 121111(R) (2014).
- [36] P. Blaha, K. Schwarz, G. K. H. Madsen, D. Kvasnicka, and J. Luitz, *WIEN2k, An Augmented Plane Wave + Local Orbitals Program for Calculating Crystal Properties* (Technische Universität Wien, Austria, 2001); P. Blaha, K. Schwarz, P. Sorantin, and S. Trickey, *Comput. Phys. Commun.* **59**, 399 (1990).
- [37] N. Marzari and D. Vanderbilt, *Phys. Rev. B* **56**, 12847 (1997).
- [38] For the Wannier90 code, see A. A. Mostofi, J. R. Yates, Y.-S. Lee, I. Souza, D. Vanderbilt, and N. Marzari, *Comput. Phys. Commun.* **178**, 685 (2008); for the interface to WIEN2K, see J. Kuneš, R. Arita, P. Wissgott, A. Toschi, H. Ikeda, and K. Held, *ibid.* **181**, 1888 (2010).
- [39] For a pedagogical presentation see, e.g., E. Pavarini, The LDA+DMFT Approach, in *The LDA+DMFT Approach to Strongly Correlated Materials*, edited by E. Pavarini, E. Koch, D. Vollhardt, and A. Lichtenstein, Modeling and Simulation, Vol. 1 (Forschungszentrum Jülich, Jülich, 2011), <http://www.cond-mat.de/events/correl11/manuscripts/pavarini.pdf>.
- [40] P. Liu, B. Kim, X. Q. Chen, D. D. Sarma, G. Kresse, and C. Franchini, *Phys. Rev. Mater.* **2**, 075003 (2018).
- [41] T. Shimura, Y. Inaguma, T. Nakamura, M. Itoh, and Y. Morii, *Phys. Rev. B* **52**, 9143 (1995).
- [42] G. Zhang and E. Pavarini (unpublished).
- [43] S. Zhou, K. Jiang, H. Chen, and Z. Wang, *Phys. Rev. X* **7**, 041018 (2017).
- [44] H. Watanabe, T. Shirakawa, and S. Yunoki, *Phys. Rev. Lett.* **105**, 216410 (2010).
- [45] H. Watanabe, T. Shirakawa, and S. Yunoki, *Phys. Rev. B* **89**, 165115 (2014).

- [46] E. Gorelov, M. Karolak, T. O. Wehling, F. Lechermann, A. I. Lichtenstein, and E. Pavarini, *Phys. Rev. Lett.* **104**, 226401 (2010).
- [47] G. Zhang and E. Pavarini, *Phys. Rev. B* **95**, 075145 (2017).
- [48] G. Zhang and E. Pavarini, *Phys. Rev. B* **99**, 125102 (2019).
- [49] G. Zhang, E. Gorelov, E. Sarvestani, and E. Pavarini, *Phys. Rev. Lett.* **116**, 106402 (2016).
- [50] G. Zhang and E. Pavarini, *Phys. Status Solidi RRL* **12**, 1800211 (2018).
- [51] E. Sarvestani, G. Zhang, E. Gorelov, and E. Pavarini, *Phys. Rev. B* **97**, 085141 (2018).
- [52] I. Dzyaloshinsky, *J. Phys. Chem. Solids* **4**, 241 (1958).
- [53] B. J. Kim, H. Ohsumi, T. Komesu, S. Sakai, T. Morita, H. Takagi, and T. Arima, *Science* **323**, 6 (2009).
- [54] F. Ye, S. Chi, B. C. Chakoumakos, J. A. Fernandez-Baca, T. Qi, and G. Cao, *Phys. Rev. B* **87**, 140406(R) (2013).
- [55] N. S. Headings, S. M. Hayden, R. Coldea, and T. G. Perring, *Phys. Rev. Lett.* **105**, 247001 (2010).
- [56] A. A. Katanin and A. P. Kampf, *Phys. Rev. B* **66**, 100403(R) (2002).
- [57] A. A. Katanin and A. P. Kampf, *Phys. Rev. B* **67**, 100404(R) (2003).
- [58] A. M. Toader, J. P. Goff, M. Roger, N. Shannon, J. R. Stewart, and M. Enderle, *Phys. Rev. Lett.* **94**, 197202 (2005).
- [59] C. B. Larsen, A. T. Rømer, S. Janas, F. Treue, B. Mørnsted, N. E. Shaik, H. M. Rønnow, and K. Lefmann, *Phys. Rev. B* **99**, 054432 (2019).
- [60] K. Majumdar, D. Furton, and G. S. Uhrig, *Phys. Rev. B* **85**, 144420 (2012).
- [61] M. Takahashi, *J. Phys. C* **10**, 1289 (1977).
- [62] J. Kim, A. H. Said, D. Casa, M. H. Upton, T. Gog, M. Daghofer, G. Jackeli, J. van den Brink, G. Khaliullin, and B. J. Kim, *Phys. Rev. Lett.* **109**, 157402 (2012).
- [63] www.gauss-centre.eu.
- [64] P. A. M. Dirac, *Proc. R. Soc. A* **123**, 714 (1929).
- [65] M. Roger, *J. Phys. Chem. Solids* **66**, 1412 (2005).
- [66] D. J. Thouless, *Proc. Phys. Soc. London* **86**, 893 (1965).